



Phase transition and changing properties of nanostructured V_2O_5 thin films deposited by spray pyrolysis technique, as a function of tungsten dopant

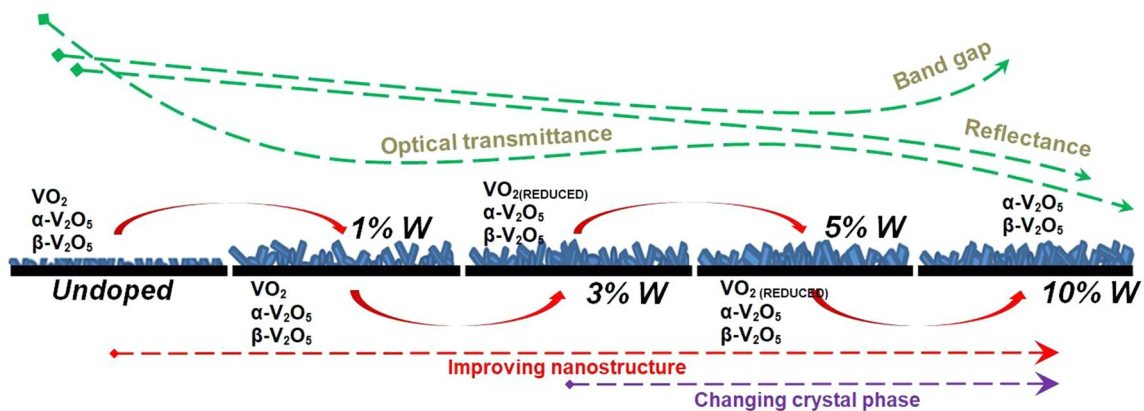
Ali Baltakesmez¹ · Cengiz Aykaç² · Betül Güzeldir²

Received: 15 January 2019 / Accepted: 25 May 2019 / Published online: 29 May 2019
© Springer-Verlag GmbH Germany, part of Springer Nature 2019

Abstract

To investigate their formation mechanism and basic electronic behaviors, in this study undoped and tungsten (W)-doped vanadium oxide films were comparatively analyzed by X-ray diffraction (XRD), scanning electron microscopy (SEM), atomic force microscopy (AFM), Raman spectroscopy, photoluminescence (PL) and UV–Vis spectroscopy. The XRD measurement showed that the W doping causes a change in crystalline phase, improvement of grain size, a decrease in dislocation and stress with different dopant ratios. The SEM and AFM images evidenced that the W-doped films change nanostructured form from nanorods to composition of nanorods and nanoplates at 400 °C, which is 20% lower than general formation temperature of vanadium pentoxide (V_2O_5) nanorods, while the undoped film have small-sized nanostructural morphology as an initial stage. The Raman spectrum also indicates significant changes of its structural and optical properties. The PL quenching is observed in the PL spectra of the W-doped V_2O_5 films with decreasing deep-level emission. Band gap, Urbach energy, reflective index and dielectric constant of all the films were calculated by data of the UV–Vis and reflectance measurements. The results showed that the W-doped V_2O_5 films were more suitable for (opto)electronic device applications such as solar cell, gas sensor, electrochromic electrode and battery.

Graphic abstract



✉ Ali Baltakesmez
alibaltakesmez@ardahan.edu.tr

¹ Department of Electricity and Energy, Technical Scientific Vocational School, Ardahan University, 75000 Ardahan, Turkey

² Department of Physics, Faculty of Sciences, Atatürk University, 25240 Erzurum, Turkey

1 Introduction

Recently, the vanadium oxides as a class of semiconducting oxides, VO, V_2O_3 , VO_2 and V_2O_5 including in the V^{2+} , V^{3+} , V^{4+} and V^{5+} oxidation states, are remarkable due to their typical properties for various technological applications. Foremost among them, the V_2O_5 as a transition-metal oxide

n-type semiconductor is one of the remarkable candidates due to wide band gap (2.4–2.8 eV), high absorption coefficients, thermal stability, multivalence layered structure, abundance, low cost and electrochromic and photocatalytic feature [1–3]. These properties allow this material's entry into the (opto) electronic applications such as solar cells [4], light emitting diodes [5], photodiodes [6], transistors [7], gas sensors [8], electrochromic devices [9] and solid-state batteries [10].

However, some disadvantages of the V_2O_5 has been reported in the previously studies such as low conductivity, which is most important one of them, for all applications and weak retention capacity in the long-term cycling conditions for storage applications [11, 12]. On the other hand, orthorhombic structure of the V_2O_5 (α - V_2O_5) has been generally reported due to most stable form and its suitable properties for the applications [13, 14]. However, the activation energy of conductivity is 0.24 and 0.1 eV at near room temperature for α - and β - V_2O_5 (tetragonal structure), respectively [15, 16]. Therefore, the β - V_2O_5 is more suitable for conductivity while α - V_2O_5 is useful for long-term working conditions. Thus, the mixed phase of V_2O_5 may be solution for the above-mentioned problems.

In addition to the issues of the applications, as reported by many authors, V_2O_5 thin films have generally amorphous structure when deposited at low growth temperatures (≤ 300 °C) [17–20]. Furthermore, it is emphasized that formation temperature (growth, annealing and post-annealing) of nanostructured V_2O_5 is 400 °C for starting and to be completed about 550 °C [21]. It is well known that low temperature processes using fabrication of (opto)electronic devices is the desired condition. On the other hand, due to changeable transfer temperature and electrical and optical properties, vanadium oxide has been doped with various dopants such as tungsten (W), molybdenum (Mo), niobium (Nb), fluorine (F), iron (Fe) and chromium (Cr) [22–27]. For example, Zheng et al. [28] have reported W-doped V_2O_5 nanobelts have higher specific capacitance than the previous values of V_2O_5 materials for due to excellent electrochemical property, high specific capacitance and good rate capability. Chen et al. [29] have used the Mo to investigation of effect on phase transition temperature of VO_2 nanopowders and showed decreasing phase transition temperature in the Mo doped VO_2 . On the other hand, F doped V_2O_5 films having tetragonal β - V_2O_5 phase have been reported by Mousavi et al. [25]. In this study, while the size of nanostructures decreased with increasing F doping level, the width of nanostructure increased. Also, resistivity, transparency and optical band gap of the films decreased in the F doped films. Finally, impurity cations into vanadium oxide lattice can change structural, morphological, electrical and optical properties of the vanadium oxide such as crystalline phase, shape of nanostructure, conductivity, chemical activity and color control of electrochromic electrode.

The nanostructured V_2O_5 thin films can be obtained by several growth techniques such as thermal evaporation [30], pulsed laser deposition (PLD) [31], magnetron sputtering [32], sol–gel process [33], chemical vapor deposition [34], electron beam evaporation [35], and spray pyrolysis [36]. The chemical spray pyrolysis (CSP) is an advantageous method for preparation of thin films coated on large area due to being simple and inexpensive process. Furthermore, the CSP deposition technique offers crucial advantages such as control of stoichiometry and thin film structure [37].

In this study, undoped (reference sample) and W-doped vanadium oxide thin films deposited by the CSP at same preparation conditions was investigated. Structural, morphological and optical properties of the thin films were determined and comparatively discussed.

2 Experimental details and measurements

Microscope glass slides as glass substrate were purchased from Isolab/Germany. Before cleaning and film growth, the glass slides were cut to smaller pieces of 1.5 cm \times 1.5 cm. Thickness of the glass substrates is 0.4 cm and the substrates were used without surface polishing. The EDX analysis was conducted to determine of composition of the glass substrates and is given in Fig. 5a. The chemical salts of vanadium trichloride (VCl_3) (97% purity) and tungsten hexachloride (WCl_6) (99.9% purity) were purchased from ACROS Organics and abcr (Gute Chemie), respectively. All the depositions were carried out by compressed purified air of 2 bar (1.97 atm.) pressure as the carrier gas with 5 ml/min solution flow at vertical position of spray-nozzle. Purified air was used as the carrier gas and the distance between spray-nozzle and glass substrate was set 30 cm in all the deposition process. The chemical solvents used were purchased from Sigma-Aldrich and used without post-treatment.

The glass substrates were cleaned as follows: Firstly, substrates in acetone were waited in ultrasonic bath for 15 min and washed with deionized water and then dried with N_2 gas flow. Secondly, they were chemically cleaned in 10% NaOH solution pre-heated up to 55 °C and finally, substrates in deionized water were hold in ultrasonic bath for 15 min and then dried with N_2 gas flow, respectively.

The undoped V_2O_5 thin films were deposited by precursor solutions prepared with 0.05 M (393 mg) VCl_3 in 50 ml deionized water. On the other hand, the doped V_2O_5 thin films were deposited by the precursor solution including percentage weight ratios (wt%) of 1, 3, 5 and 10 WCl_6 , 4 mg (0.31 mM), 12 mg (0.63 mM), 20 mg (1.57 mM) and 40 mg (3.14 mM), respectively. After the precursor solution was stirred for 60 min at room temperature (RT), the thin films were deposited on the glass substrates by spray pyrolysis technique at 300 °C for 20 min and naturally cooled to RT.

After then, the undoped and the W-doped V₂O₅ thin films were post-annealed in air at 400 °C for 60 min without heating and cooling step. A photograph of the HOMARC Spray Pyrolysis Equipment and growth control parameters are given in Fig. 1. After the post-annealing process, the V₂O₅ thin films were characterized.

The crystallinity of the films was checked using Bruker D2 PHASER X-ray diffraction (XRD) system with CuK_α radiation at $\lambda = 1.54184 \text{ \AA}$. The images of field emission scanning electron microscopy (FE-SEM) including cross-sectional and atomic force microscopy (AFM) to reveal morphological properties were obtained using a system of ZEISS Sigma 300 and Hitachi 5100 N, respectively. Energy dispersive X-ray (EDX) analysis for compositional analysis was conducted with measurement system of ZEISS Sigma 300 equipped with EDX spectroscopy. Raman spectra were recorded using a μ -Raman/PL spectrometer of WITEC Alfa 300R. The excitation source is a He–Ne laser with an excitation wavelength of 531.96 nm. The photoluminescence (PL) spectra were obtained using Horiba in the wavelength range of 350–900 nm. A Perkin-Elmer Lambda2S UV–visible spectrometer was used in order to obtain absorption and calculate the band gaps of the films. The film thickness was determined using a surface profilometer (KLA Tencor P7).

3 Results and discussion

3.1 Structural analysis

Figure 2 shows the XRD patterns of the undoped film (a) and the W-doped films depending on dopant concentration (b–e), respectively. Figure 2a shows that the undoped film as reference sample has mixture crystal structure of monoclinic VO₂, orthorhombic V₂O₅ and tetragonal V₂O₅. Besides, high preferential orientations of (200) and (101) are stronger than that of other peaks indicating that the crystallinity

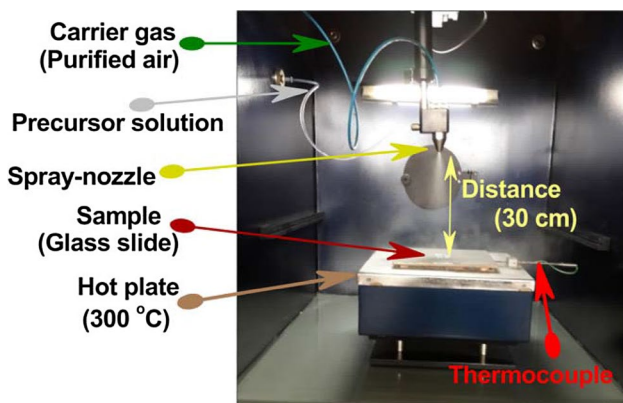


Fig. 1 A photograph of spray pyrolysis system used in this study

of undoped sample is dominantly formed α - and β -V₂O₅ phases. It exhibits characteristic 2θ values of 12.55, 14.24, 26.79, 31.42 and 42.64 with respective Miller indices (200), (002), (330), (242) and (003), which are consistent with crystalline the β -V₂O₅ phase and are in good agreement with the JCPDS card No. 045-1074 (crystal system: Tetragonal, space group: PE). The appearance of (101), (201) and (012) crystal plane at 2θ values of 20.82, 25.25 and 48.81 illustrates the formation of the α -V₂O₅ crystals given in JCPDS (089-2482) (crystal system: Orthorhombic, space group: Pmmn (59)). On the other hand, weak diffraction peaks are also seen at 23.80, 25.25, 31.19 and 48.81, which matched with the (201), (110), (111) and (402) planes of the VO₂ given in JCPDS (071-0042) (crystal system: Monoclinic, space group: C2/m (12)). Besides, the XRD patterns clearly indicate the broad background at 2θ between 17° and 40° due to the amorphous feature of glass substrate.

Interestingly, the other XRD patterns show that the W-doped thin films have significant structural changes. It can be seen in Fig. 2b that the XRD pattern of the thin film doped at 1 wt% have new diffraction peaks with decreased intensity. The weak XRD intensities of the crystallite reflected plane directions are due to the nano-crystallinity [38]. However, no reflections attributable to compounds deriving from the dopant elements were observed. It suggests that precursor solution of the V₂O₅ with homogeneously dispersed the W dopant is successfully prepared. For the peak of preferential orientation along (200), the full-width half-maximum (FWHM) value is dramatically decreased from 0.345 to 0.130. This structural change can be attributed that the crystallinity and crystalline structures in the film is enhanced, leading to the higher lattice order. However, the existence of three crystal phases is not affected and the β -V₂O₅ phase has become prominent. Furthermore, the increasing dissimilar orientations of phases in the XRD pattern can be attributed to that the dopant induced the change in crystal growth and then reorientation of crystallinity plane. The secondary dominant α -V₂O₅ peak disappeared after the doping process. Besides, the predominant peak center significantly shifted towards lower diffraction angle, from 12.549° to 12.511°.

After doping at 3 wt% (Fig. 2c), the (200) β -phase peak still dominated in the XRD spectrum with decreased intensity, indicating that the degree of (200) preferential orientation decreased with increasing doping concentration due to substitution of W ions in V₂O₅ lattice making O ions move to interstitial sites and resulting in a less ordered crystalline phase. In addition to this result, the (400), (241) and (233) β -phase peaks are more sharpened with higher intensity, while the intensities of α -phase and VO₂ diffraction peaks are getting weaker. The formation of the increasing β -V₂O₅ phase at 3 wt% can be due to the improving chemical reactions for various crystalline

Fig. 2 XRD patterns of the pure (a) and doped thin films with the W rate of 1 wt% (b), 3 wt% (c), 5 wt% (d) and 10 wt% (e)

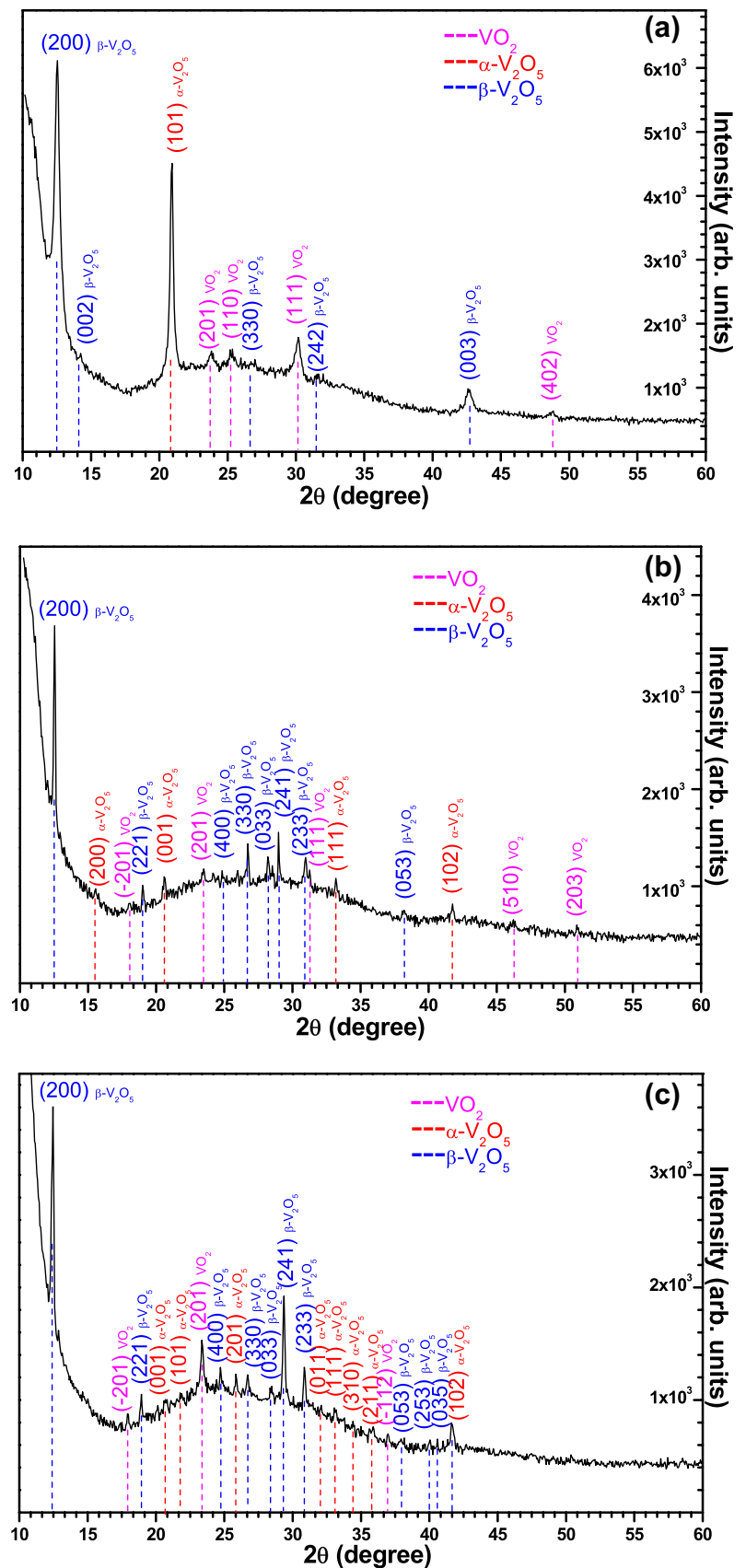
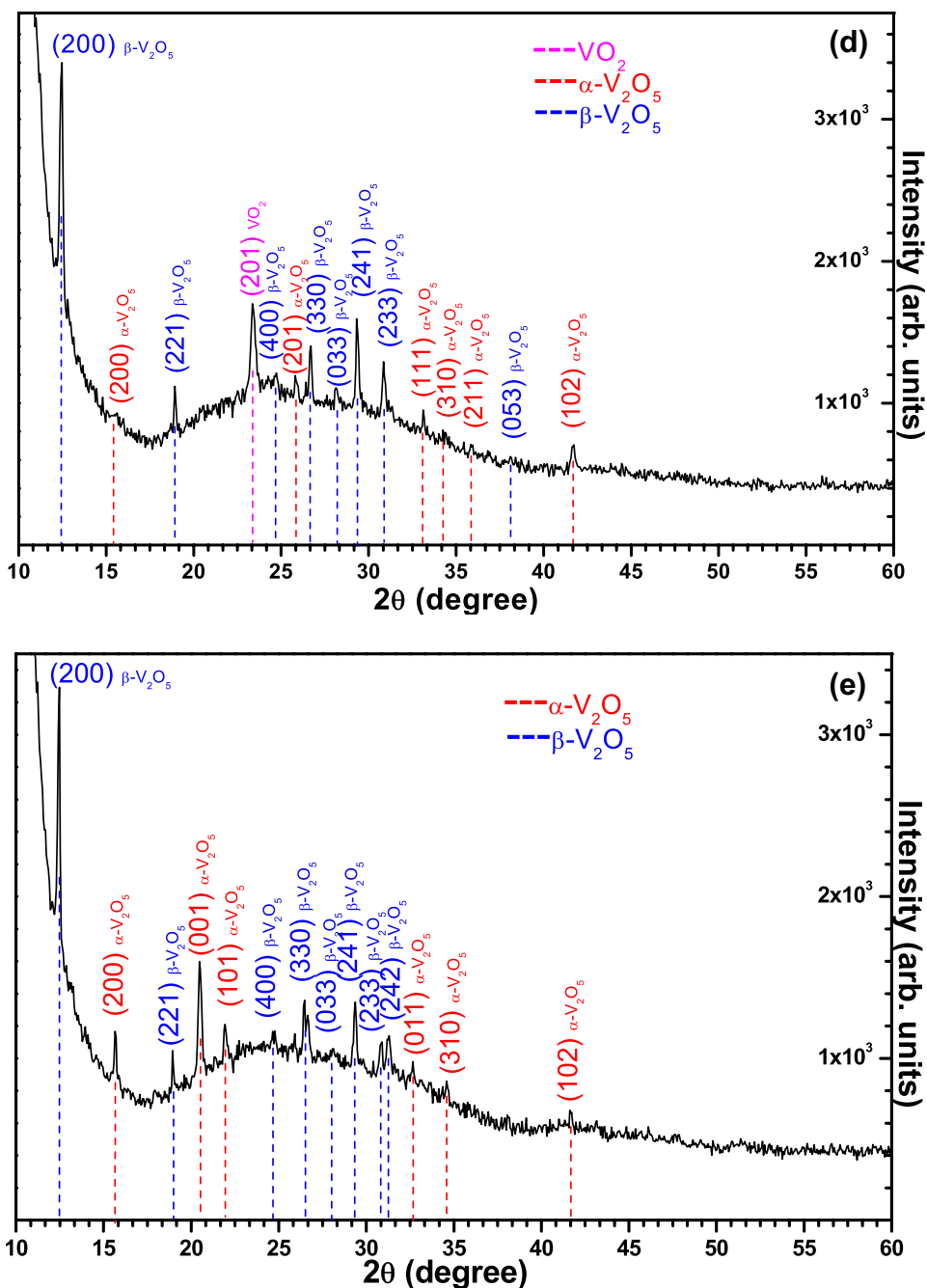


Fig. 2 (continued)



orientations in the annealing process. It can be evident that the doping at 3 wt% affected crystalline orientation rather than quality because the FWHM value of preferential orientation along (200) was nearly same value of 0.131 while peak center was shifted towards lower diffraction angle, from 12.511° to 12.499° . In the theory, original XRD peak positions and peak intensities of a doped structure with other atoms change due to the repeat distances in the lattice structure arising from the different size between host and doped atoms and difference in electron density of the doped atom, respectively [39]. Therefore, the changing

intensity, angle and orientation of diffraction peaks evidence that our dopant incorporated successfully.

Furthermore, for the film prepared with 5 wt% W including precursor solution, the XRD pattern in Fig. 2d demonstrates a more decreased intensity of (200) peak and shifted 2θ position towards 12.463° . Specifically, the XRD data suggests that the diffraction peaks of monoclinic VO_2 secondary phase nearly disappeared, except its (201) plane. Besides, the number of diffraction planes decreased while intensity generally increased in the XRD pattern. The appeared dominant V_2O_5 phase with increasing dopant level can be due to enhanced

oxygen chemisorption, which is considered as filled oxygen vacancies in the lattice by oxygen through gas phase oxidation. On the other hand, Fig. 2e presents the XRD pattern of the film obtained from 10 wt% W-loaded solution. As seen in Fig. 2e, the monoclinic VO₂ secondary phase fully disappeared and only V₂O₅ phase reflection peaks were observed. This change may be attributed to that tensile stress will be helpful to the phase transition occurring at the lower temperature because its volume expands by 1% of its original volume when vanadium dioxide changes from a semiconducting state to a metal state [40]. In addition, shifting degree of the 2θ position at (002) is bigger than the other, as seen in Table 1. In this regard, the W dopant induced the change in crystal phase, crystalline quality and reorientation planes are clearly evident from their XRD patterns. In addition to the relevant phase changes mainly occurred, microstructural parameters like crystallite size, strain and dislocation density positively were affected. The parameters were calculated from the (200) XRD peak of β-V₂O₅ phase and given in Table 1.

The grain size along the preferred orientation of β-V₂O₅ peak was calculated by using the Scherrer's equation:

$$D = \frac{K\lambda}{\beta \cos \theta} \quad (1)$$

where D is the crystallite size, K is a dimensionless shape factor and has a typical value of about 0.9, λ is the wavelength of the incident radiation (1.5406 Å), β is the full-width half-maximum (FWHM) and θ is the Bragg's angle of diffraction. The crystallite size of W-doped films was found to be ≥ 54 nm. The best size is obtained with 1 wt% and 3 wt%, whereas the reference sample has 23.15 nm size. This result indicates that the doped films are highly crystalline. The d -spacing of W-doped V₂O₅ can be calculated by the Bragg formula: $2d \sin \theta = n\lambda$, where d is the interlayer distance. The increment of interlayer distance of the W-doped thin films was observed to be blue shifted (200) plane. Additionally, in order to have more information, the dislocation density (δ) and strain value were calculated by the formulas, respectively,

$$\delta = \frac{1}{D^2}, \quad (2)$$

$$\varepsilon = \frac{\beta \cos \theta}{4}. \quad (3)$$

It can be seen in Table 1 that the dislocation density decreases with the W dopant which may be due to decrease in concentration of lattice defects such as oxygen vacancy. However, the dislocation density increased after 3 wt% dopant. Therefore, the value of 3 wt% is critical for dislocations. This result showed that the W dopant plays a constructive role in crystallinity of the film until the critical value 3 wt%. However, the higher doping rate than the critical value may cause lattice defect due to difference of atomic parameters such as atomic radius. On the other hand, due to the increase in d -spacing (d : 7.130 Å given in JCPDS (045-1074)), the strain will be decreased in the structure.

3.2 FE-SEM and AFM analysis

Figures 3 and 4 show SEM images of the undoped and the W-doped V₂O₅ films prepared at the 1, 3, 5, 10 wt% on the glass substrate and cross-sectional images of the films, respectively. The average film thickness of 550 nm was determined by the profilometer. Also, the thicknesses determined from the cross-sectional images are 518, 569, 589, 558 and 564 nm, respectively. As seen in Fig. 3a, the undoped V₂O₅ film has grown as small seed-nanorod form. However, it can be seen in Fig. 3b that the 1 wt% W-doped V₂O₅ obtained by the same growth conditions with the undoped film have transformed into nearly uniform nanorods and interestingly diameter, length and density of the nanorods have changed by increasing W-doping concentration as seen in Fig. 3c–e. The diameter_(min-max)/length_(min-max) of the nanorods were determined by the FE-SEM system (not given in here) as 60_{min}–200_{max} nm/150_{min}–430_{max} nm, 90_{min}–520_{max} nm/320_{min}–2060_{max} nm, 150_{min}–630_{max} nm/350_{min}–2000_{max} nm, 120_{min}–720_{max} nm/320_{min}–1800_{max} nm and 120_{min}–720_{max} nm/260_{min}–1140_{max} nm, respectively. This alteration suggests that the form of the W-doped films still keeps the same shape as the undoped film while the nanostructure growth is significantly enhanced by the dopant. This enhanced nanostructural morphology provide an advantage as a more suitable sensitive area and bigger

Table 1 Determined and calculated parameters from the XRD patterns of all the films

	Peak position (2θ)	Phases	d -spacing (Å)	FWHM	Grain size (nm)	Dislocation density ($\times 10^{-3}$ nm ⁻²)	Strain (line ⁻² m ⁻⁴)
VO	12.549	VO ₂ , α-V ₂ O ₅ , β-V ₂ O ₅	7.051	0.345	23.15	1.865	0.085
VO-1%	12.511	VO ₂ , α-V ₂ O ₅ , β-V ₂ O ₅	7.072	0.130	61.48	0.265	0.032
VO-3%	12.499	VO _{2(reduced)} , α-V ₂ O ₅ , β-V ₂ O ₅	7.079	0.131	61.01	0.268	0.032
VO-5%	12.463	VO _{2(reduced)} , α-V ₂ O ₅ , β-V ₂ O ₅	7.099	0.144	55.50	0.324	0.033
VO-10%	12.452	α-V ₂ O ₅ , β-V ₂ O ₅	7.106	0.148	54.01	0.342	0.034

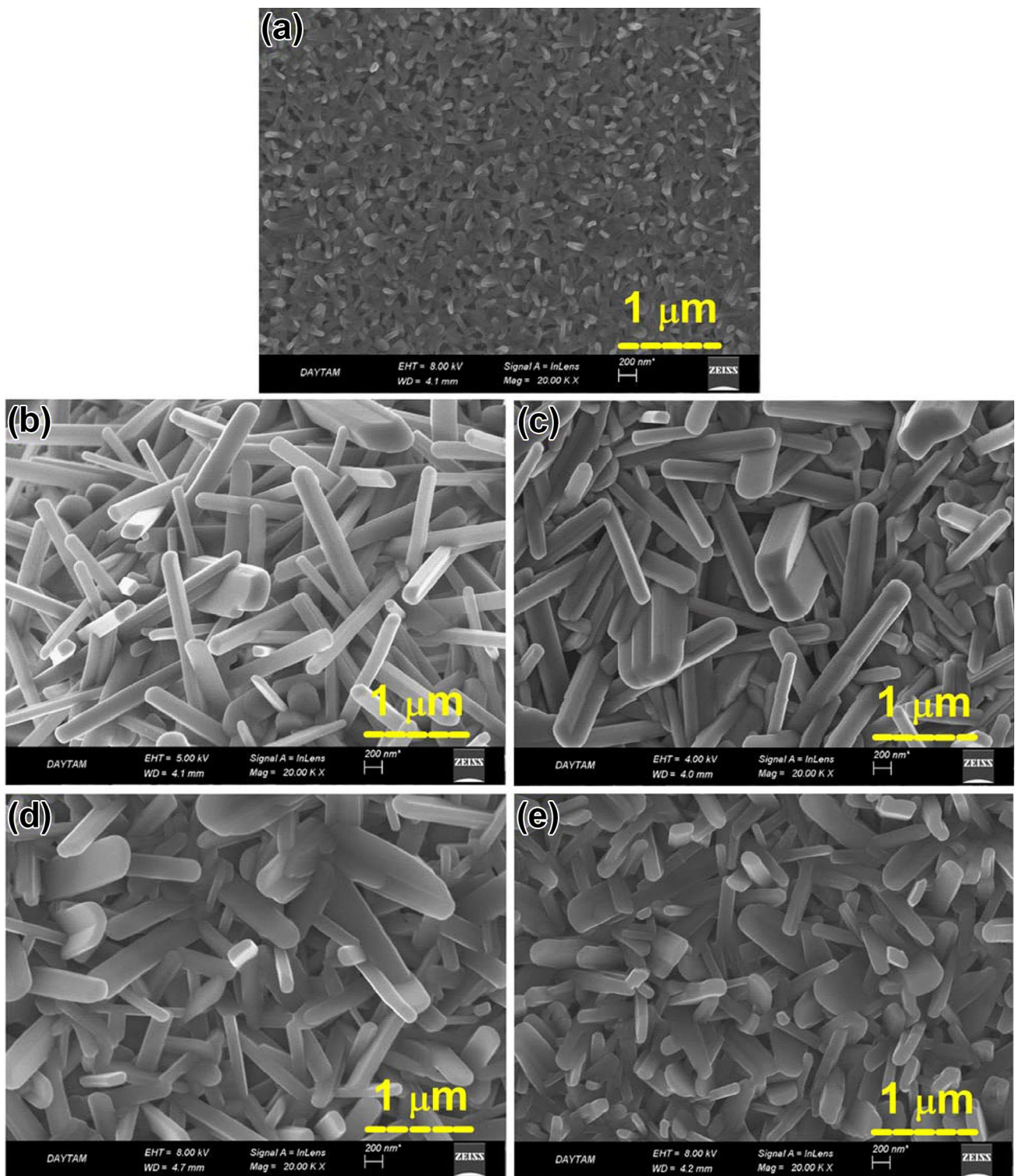


Fig. 3 SEM images of the pure (a) and 1, 3, 5 and 10 wt% W-doped V₂O₅ thin films (b–e), respectively

interlayer space for device applications such as an effective active layer for gas sensors [41], a hole transport layer for solar cells [42], and a cathode material for lithium batteries [42, 43]. In addition, it is frequently reported that film

oxidized into VO₂ phase at 300 °C, V₆O₁₃ phase at 350 °C, finally V₂O₅ at 400 °C with starting to grow nanorods structures, and transformed into V₂O₅ nanorods in the higher temperatures [44, 45]. Therefore, minimum required

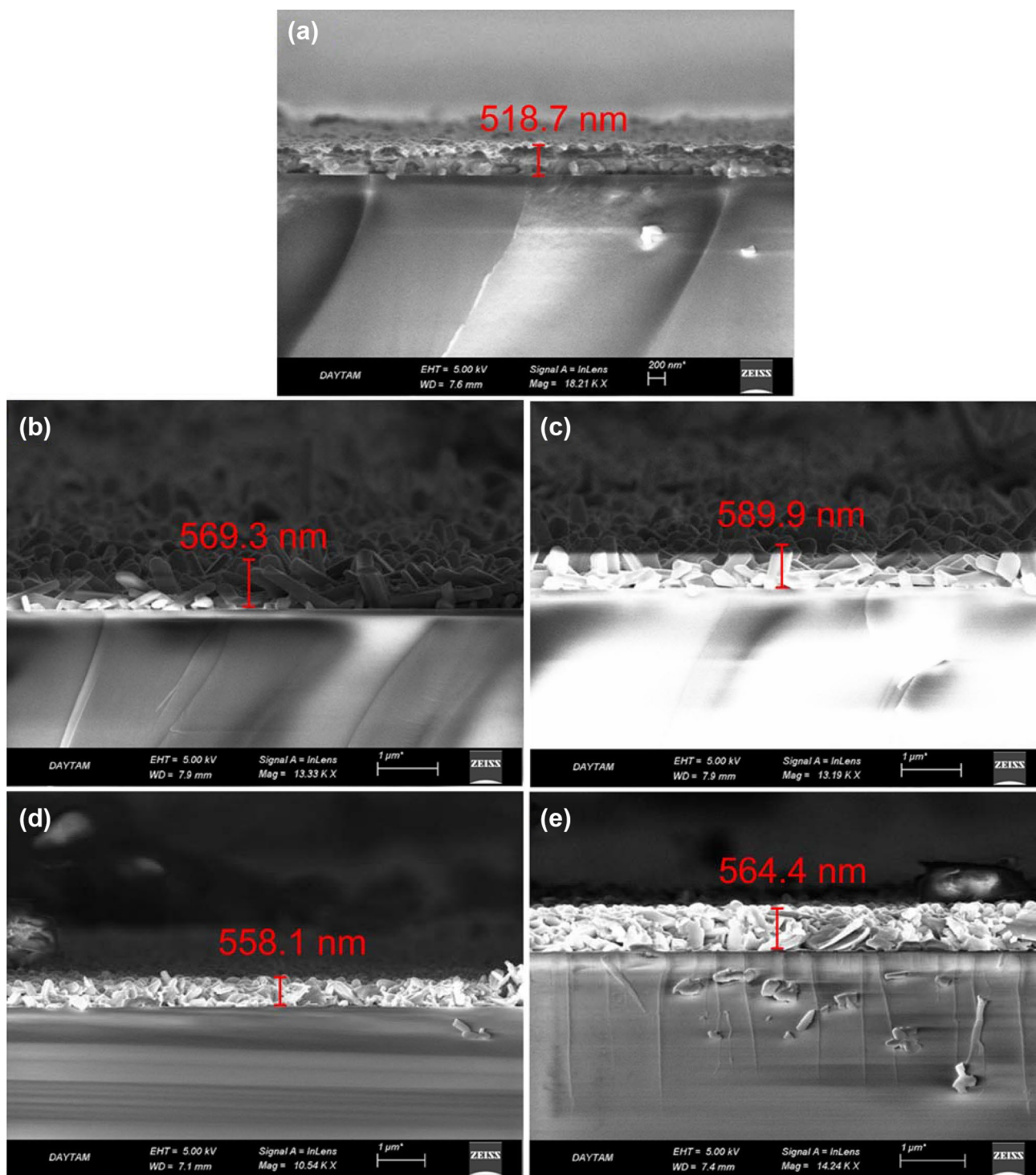


Fig. 4 Cross-sectional SEM images of the pure (a) and 1, 3, 5 and 10 wt% W-doped V_2O_5 thin films (b–e), respectively

temperature is decreased with the W doping from ≥ 500 to 400°C in this study.

On the other hand, the nanostructural morphology is gradually changed from rod to plate with the increasing dopant amount and then a composition of nanorod- and

nanoplate-shaped forms occur. Hence, the corresponding approximate ratio of the diameter_{\min} – length_{\max} is undulated as 0.139, 0.044, 0.075, 0.066 and 0.105, respectively. As clearly seen in Figs. 3 and 4, in the 3 wt% W-doped film, the nanorods having high size combine with each other to

form nanoplate, and thus, a decrease occurs from 0.075 to 0.066 in the ratio of diameter_{min} and length_{max}. Furthermore, this undulation in the values confirms that as the nanorods combine with each other to form nanoplates, the density of nanostructures is decreased with the increasing W concentration. It may be noticed that the W-doping process strongly influenced crystallization of the film. This result also suggests that the surface diffusion phenomenon which plays an important role in the growth process of nanorods due to the high dependence on the oxygen absorption is enhanced with the W dopant. It may cause that electron affinity of the W metal atoms (electronegativity: 2.36, electron affinity: 78.6 kJ/mol) is bigger than that of V atoms (electronegativity: 1.63, electron affinity: 50.6 kJ/mol) and then the increased nanorod-size can be obtained with enhanced absorption of O₂. In other words, all the specific physical and chemical properties of materials are associated with their atomic structures. The atomic structures of materials are related to atomic parameters such as lattice structure, lattice parameters, radius, growing shape and electron affinity of atoms. Additionally, the above-mentioned properties of materials are strongly based on metal concentration and type of metal in materials [46]. Figure 5b–f shows the EDX spectra of the undoped and W-doped films, respectively. The EDX analysis carried out to verify the W incorporation shows the presence of the three main elements V, O and W. According to the chemical composition of the doped films, the percentages of the W are 0.56 wt%, 2.63 wt%, 3.78 wt% and 5.86 wt%, respectively. Although the EDX analysis is used for elemental analyses only, the percentages of the W show decreasing doping efficiency with increasing doping ratio. On the other hand, atomic percentage values of the elements in the undoped and doped films are 45.51 and 54.49; 33.22, 66.67 and 0.11; 32.55, 66.92 and 0.53; 38.78, 60.54 and 0.68; 30.09, 68.83 and 1.08, respectively, for V, O and W.

The surface topology of the nanostructured films prepared with and without the dopant was analyzed using AFM in the tapping mode. Figure 6 shows 3D AFM images of the V₂O₅ nanostructured films. It was observed that the SEM and AFM analyses were consistent with the analysis of the nanostructured crystal distributions on the surfaces of the films. The surface topography images show that the surface morphology and the nanorods size are very sensitive to the dopant ratio, as seen in SEM images. Root mean square (RMS) roughness is between 100 and 400 nm. While the roughness increased with the addition of W dopant due to increased nanorod-size, surface roughness in the films doped greater than 1 wt% W decreased due to the decreasing angle between the substrate and nanorod, which can be useful for the fabrication of V₂O₅-based (opto)-electronic devices such as solar cell, photosensor, light emitting diode and gas sensor.

It is well known that performance of these devices depend on interface area. However, carrier diffusion length limits thickness of organic or inorganic semiconductor top-layer in fabrication of the devices. On the other hand, a suitable thickness should be in order to completely cover the underlayer to prevent short circuit. Therefore, increasing surface area with decreasing roughness allows a wide range in the selection of top-layer thickness.

3.3 Raman analysis

Raman spectrum analysis of undoped and W-doped V₂O₅ for all concentrations of the dopant ion is presented in Fig. 7. In addition to the other analyses, these spectra suggested that the films have orthorhombic structure of V₂O₅. Also, applying the W dopant influenced the crystallinity of the V₂O₅ nanorods. The Raman spectrum consists of two groups of peaks, the peaks located at higher frequency region are called internal modes and the ones in low-frequency region are called external modes [47]. The Raman peaks located at 140.75, 201.62, 260.75, 279.92, 403.54, 481.59, 506.54, 692.81, and 996.67 cm⁻¹ were indexed to the V₂O₅ crystal. On the other hand, the signal peak at 260.75 cm⁻¹ is assigned to the VO₂ phase with vibrational modes of V–O bonds [48].

The predominant low-wavenumber band at 140.75 cm⁻¹ is attributed to the skeleton bent vibration related to B_{3g} symmetry vibration that is an evidence for the layered structure of V₂O₅ phase and nanorods [49, 50], and the peaks at 201.62 and 279.92 cm⁻¹ are from the bending vibrations of the O_C–V–O_B bond related to B_{2g} [51]. The peak at 403.54 cm⁻¹ is assigned to the bending vibrations of the V=O bonds related to A_g symmetry vibration. The bending vibration signal of V–O–V doubly coordinated oxygen is observed at 481.59 cm⁻¹. The peak at 506.54 cm⁻¹ is assigned to the triply coordinated oxygen (V₃–O) stretching modes related to A_g symmetry vibration. The peak at 692.81 cm⁻¹ is assigned to the doubly coordinated oxygen (V₂–O) stretching and bending vibrational modes related to B_{2g} symmetry vibration [52]. The peak at 996.67 cm⁻¹ corresponds to the terminal oxygen (V₅–O) stretching mode related to A_g symmetry vibration, and also associated to the crystallinity quality and stoichiometry of the layered structure of V₂O₅ nanorods [53]. In the case of the Raman peaks at 523 and 696 cm⁻¹, they are attributed to V₃–O phonon band and V–O–V modes. Intensity of both these modes was found to be quite small [54].

Clearly, the Raman analysis is in accord with the XRD patterns. As seen the Raman spectra, in the 5 wt% W-doped thin film, the weaker mode intensity and broader stretching vibration peaks beyond 400 cm⁻¹ have been observed. It can be attributed that while the mode intensity increases with increasing dominant V₂O₅ diffraction peaks, the dominant

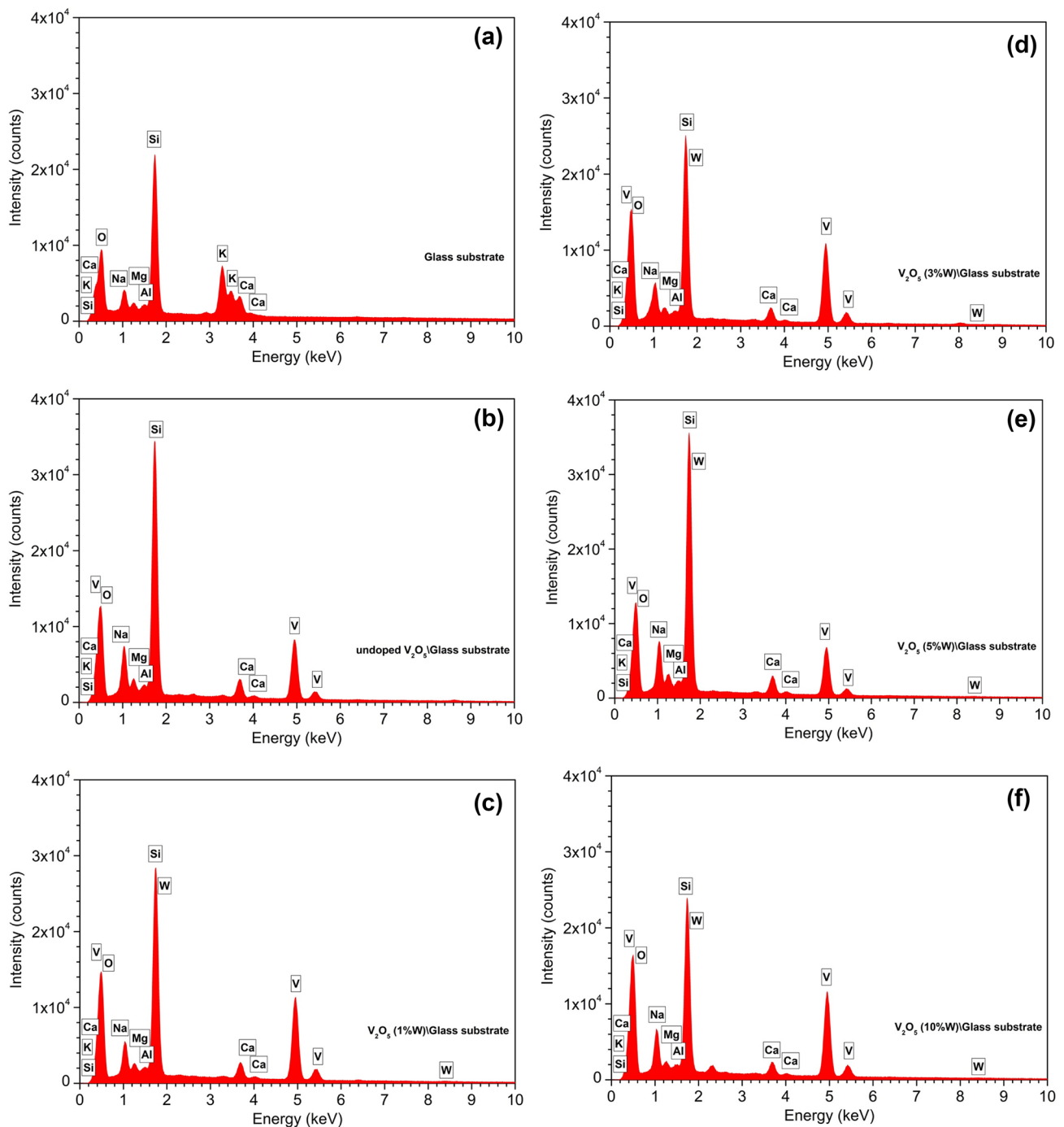


Fig. 5 EDS spectra of the glass substrate (a), undoped thin film (b) and W-doped thin films (c–f), respectively

diffraction peaks of the VO_2 caused the broad spectrum with weaker intensity.

3.4 Optical studies

Figure 8 presents the PL spectra recorded at room temperature of the undoped and the W-doped V_2O_5 thin films. In the measurement, an excitation source with wavelength

of 325 nm was used for all samples. All the samples show two luminescence mechanisms which are intrinsic and extrinsic transition centralized at the green and the red region of the electromagnetic spectrum, respectively. The broad intrinsic transition peaks around 420 and 570 nm are attributed to recombination of photo-excited pairs that are electron in bottom of conduction band as in lowest split-off V-3d and hole in top of O-2p, respectively [55].

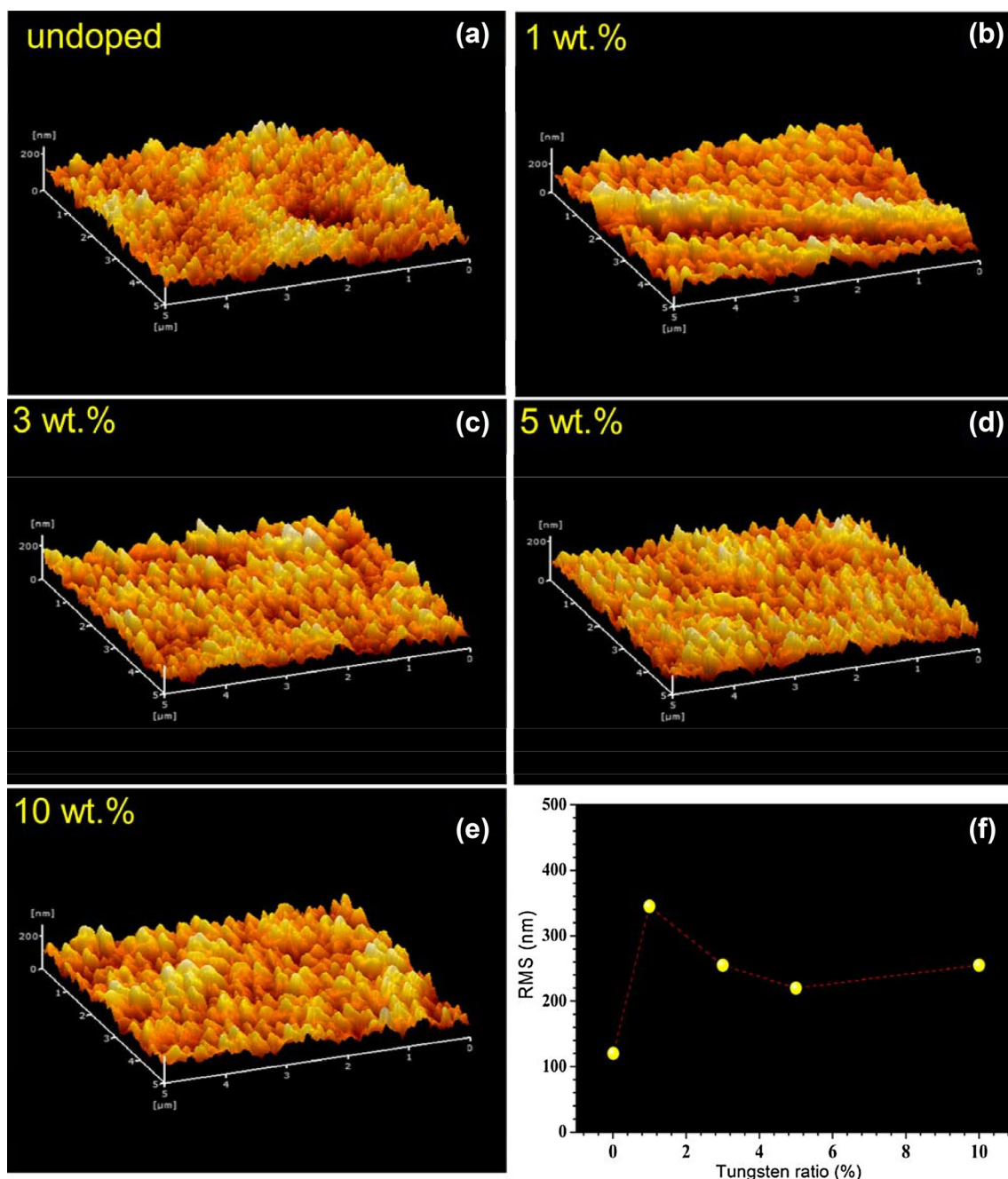


Fig. 6 AFM images of the undoped and W-doped V₂O₅ thin films, respectively, and graph of root mean square (RMS) versus the doping rate

The weak peak at 705 nm originates from formation of oxygen vacancies because defects of oxygen vacancy act as recombination center for photo-generated electron. In addition, lower wavelength peaks at 686 nm is derived from the transition from donor defect band to the 0–2p valence band. As seen in Fig. 8, for band gap values, infrared shift at the near band edge emission (NBE) peak of the W-doped V₂O₅ nanorods is in good agreement with those obtained from UV–Vis analyses. However, PL quenching

is observed at the W-loaded films compared to the undoped V₂O₅ film. With increasing length of the W-doped V₂O₅ nanorods, PL quenching might originate from increasing surface states which are generally formed in the nano-sized crystal structures because surface states may act as traps and thereby may decrease excitonic emission. Besides, the infrared shift with the W dopant indicates that excess electrons are localized at the empty orbital of V and W atoms and as a result, the band gap is decreased

Fig. 7 Raman spectra of the undoped and W-doped V_2O_5 thin films

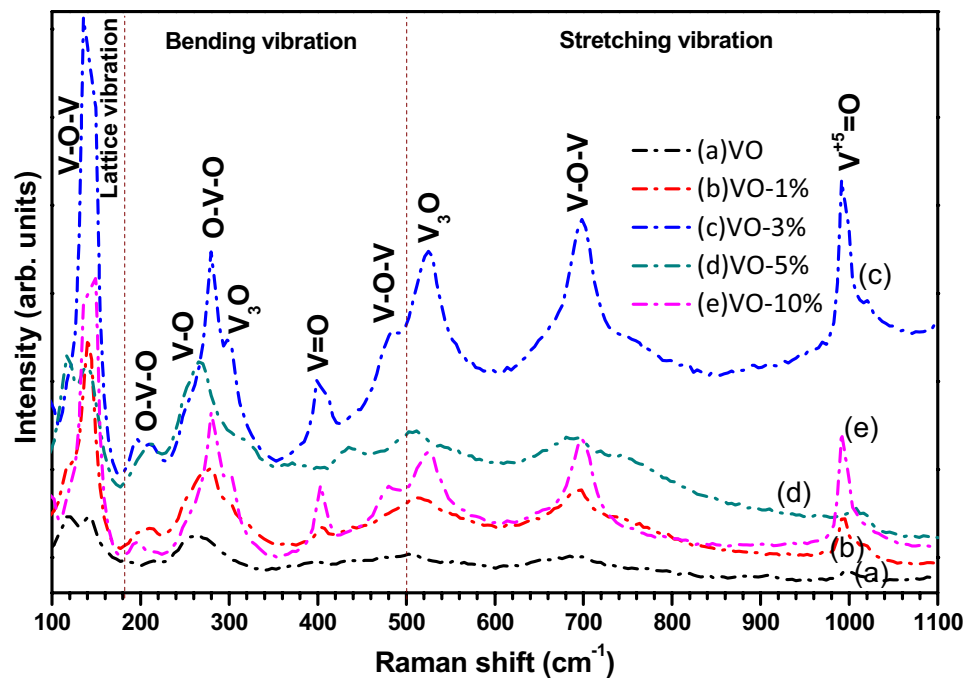
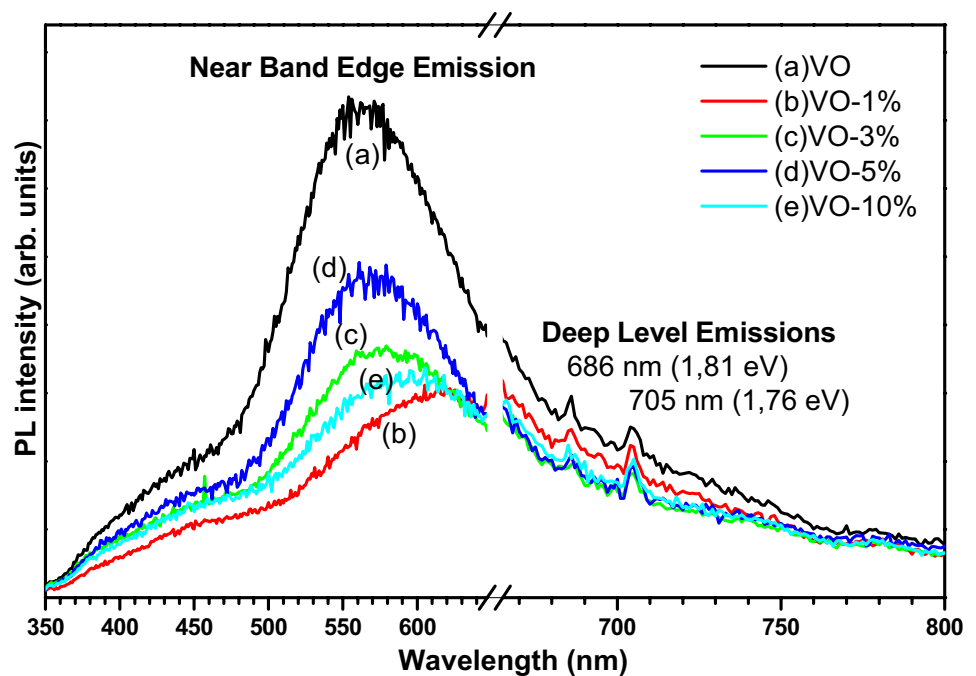


Fig. 8 Photoluminescence spectra of the undoped and doped V_2O_5 thin films



in the W-doped samples with increasing localized states in the band gap. On the other hand, the quenching intensity of the red emission peaks (deep-level emission) is attributable to decreased density of the oxygen vacancy defects in the W-doped V_2O_5 nanorods, especially for doped one at 1 wt%. This situation can be attributed to that the W dopant accelerated the absorption of oxygen at lower post-annealing temperature due to high electron negativity than V as the mentioned above.

The optical absorbance and transmittance graphs of the prepared films in the range of 1.5–3.0 eV energy are depicted in Fig. 9. The inset in Fig. 9a shows the absorption spectra of all the films in the near UV–vis region. Absorption edges of the W-doped nanostructured films shifted to lower energy values, and they, respectively, change to the shorter wavelengths for 10, 3, 5 and 1 wt% W, respectively. From the absorbance measurements, using the following equations:

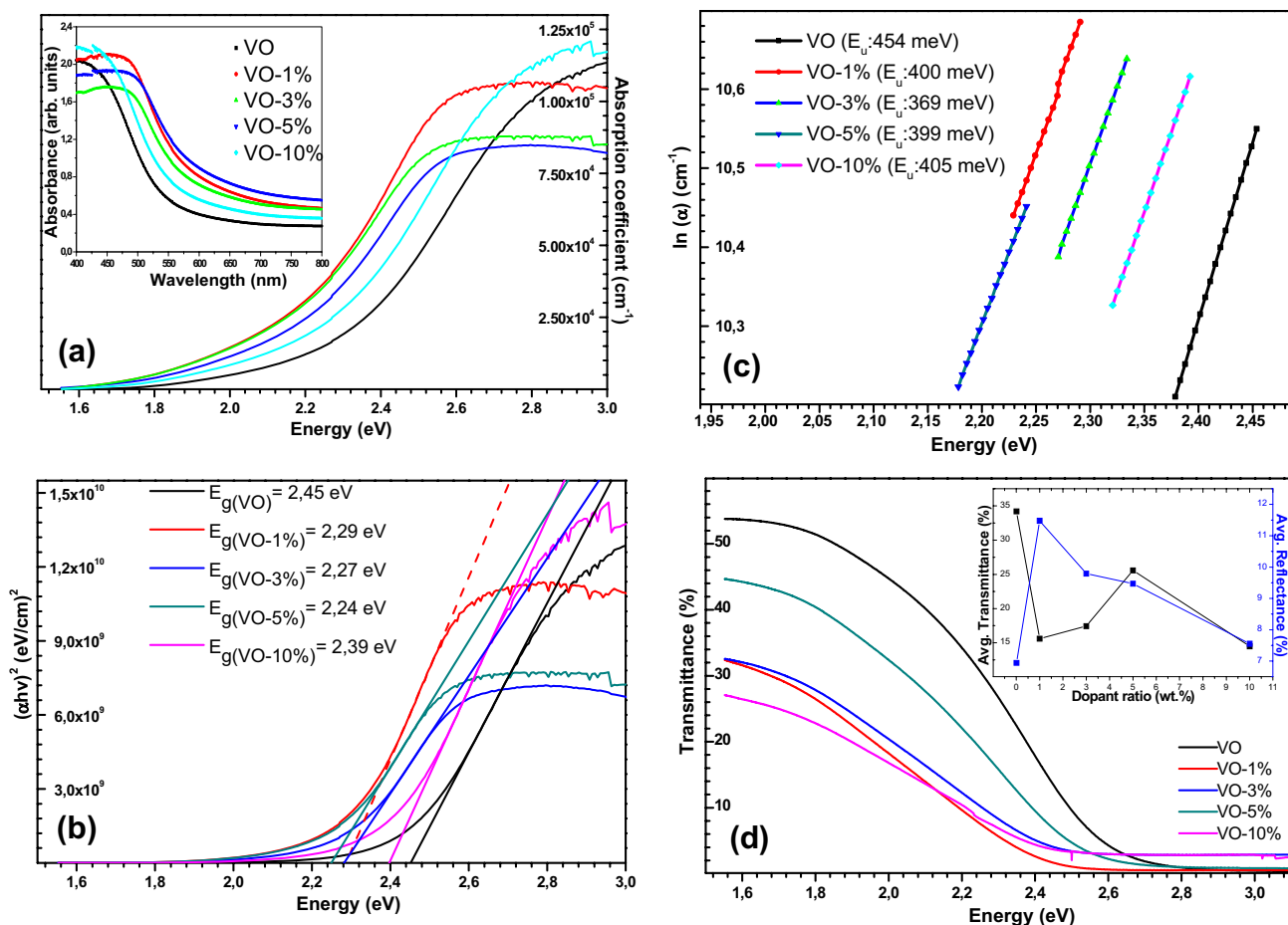


Fig. 9 The plots of absorption coefficient versus photon energy with inset UV–visible absorption spectra (a); $(\alpha h\nu)^2$ versus $h\nu$, the photon energy (b); the corresponding $\ln(\alpha)$ versus photon energy (c) and

optical transmittance (d) with inset graph of average transmittance and reflectance versus dopant ratio of the thin films, respectively

$$T = \frac{(1 - R)^2 \exp(-\alpha t)}{(1 - R^2) \exp(-2\alpha t)} = \exp(-A), \quad (4)$$

$$\alpha h\nu = K(h\nu - E_g)^{1/2}, \quad (5)$$

absorbance values are converted to absorption coefficients in order to find the band gaps of thin films from the α^2 versus $h\nu$ plots, as seen in Fig. 9b, where R is the reflectance, α is the absorption coefficient, t is the film thickness, $h\nu$ is the incident photon energy and K is the constant. Using these graphs, the calculated band gap (E_g) of the reference films is 2.45 eV, which is compatible with the reported values of the V₂O₅ film prepared by different processes. On the other hand, band gaps of the W-doped nanostructured films are narrower than that of undoped film and values are 2.29 eV, 2.27 eV, 2.24 eV and 2.39 eV according to increasing rate of W-contribution, respectively. Although the band gap values significantly reduced in the W-doped V₂O₅ films compared to the undoped V₂O₅ film, the band

gap value of the 10 wt% W-doped V₂O₅ film showed an increase. The increase in the band gap is attributed to the microstructural changes, as seen in the SEM images, and disappearance of the monoclinic VO₂ secondary phase having lower band gap energy (<1 eV) [56], as seen in the XRD pattern. Thus, the increased oxygen and electrons in the V₂O₅ lattice cause slight increase in the band gap. On the other hand, despite the VO₂ secondary phase in the undoped thin film, the band gap is larger than that in others. It can be attributed to structural and morphological properties of the undoped V₂O₅ film having the small grain size and random small-sized nanorod distribution, as seen in Table 1. Absorption behavior of semiconductors arises from its crystallinity. Crystalline defects and impurities cause weak and broad absorption region, while strong absorption edge is due to photonic excitation of band to band in the optical band gap. Furthermore, tail region of strong absorption edge inform perturbation of structure and disorder of crystal system [57]. This region is called Urbach tail and Urbach empirical rule

as relation of the absorption coefficient (α) and the photon energy ($h\nu$) can be determined as follows:

$$\alpha = \alpha_o \exp(h\nu/E_u), \quad (6)$$

where α_o is a constant, $h\nu$ is the incident photon energy and E_u is energy of the band tail (Urbach energy). From Eq. 6, the relation between plotting $\ln(\alpha)$ and $h\nu$ can be written as follows:

$$\ln \alpha = \ln \alpha_o + (h\nu/E_u). \quad (7)$$

Figure 9c shows the plot of $\ln(\alpha)$ versus $h\nu$ in the range of the Urbach tail. The values of E_u were calculated as 454 meV, 400 meV, 369 meV, 399 meV, 405 meV for the pure film and the 1, 3, 5, 10 wt% W-doped nanostructured films, respectively. These values are also evidence that the disordered atoms and defects in the structural bonding is decreased with increasing ratio of the W dopant, which is in accord with the XRD analyses, as given in Table 1. Furthermore, it is also observed in the values of E_u that the value of 3 wt% is critical for the increasing disordered atoms and defects in the structural bonding. It can be attributed to the unlike atomic radius and interconnection between nanorods, the gradually increasing dislocation density and strain in the vanadium oxide lattice with the increasing W.

Optical transmittances of the nanostructured films in the range of 1.5–3.0 eV energy are illustrated in Fig. 9d. The optical transmittance is also decreased with the W doping. The compatible change of the reflectance with the band gap is attributed to effect of “self-shadowing effect” due to enhanced nanostructure in form of the nanorods [58]. The self-shadowing mechanism leads to voiding within the nanostructured films due to ratio of the elongated columnar structure and angle of the nanorods. The band gap and average visible transmittance of the films were calculated, as given in Table 2. For the changes clearly seen, graph of average transmittance and reflectance versus dopant ratio is given in inset of Fig. 9d. Interestingly, the average transmittance showed an opposite trend with the band gap of W-doped films. This trend is attributed to the absorption coefficient (α) having relatively two distinct behaviors of the films in

Table 2 Measured and calculated basic optical values of the nanostructured films

	Band gap (eV)	Avg. transmittance (%)	Avg. reflectance (%)
VO	2.45	34.21	6.94
VO-1%	2.29	15.59	11.48
VO-3%	2.27	17.43	9.79
VO-5%	2.24	25.58	9.47
VO-10%	2.39	14.50	7.55

the region of under and above of 2.5 eV. For example, while the α of the 10% W-doped film is smaller than that the other doped films at the energies lower than 2.5 eV energy, the α at the energies higher than 2.5 eV is the greatest.

The reflectivity spectra obtained by the measurement system of the films are given in Fig. 10. As seen in Fig. 10a, the reflectance of the films varies between 4 and 14% over visible region. For similar reflectance behavior of the films, it is observed that a strong increment occurred at the low-energy region in the spectra while reflectance between 1.8 and 3.0 eV gradually increased with increasing energy. However, the reflectance increased nearly by four times and a broad increment peak occurred in the W-doped nanostructured films at about 2.5 eV. This energy is very close to the band gap value of the undoped film and then the changes of the behavior of absorbance and transmittance also can be attributed to increased reflectance at the this energy region. Furthermore, a general increment in the reflectance can be attributed to the effect of self-shadowing and increasing reflection from the nanostructured film surface.

Refractive index (n) is determined from reflectance (R) and extinction values (k) with following relation:

$$n = \frac{(1+R)}{(1-R)} + \sqrt{\frac{4R}{(1-R)^2} - k^2}, \quad (8)$$

where the extinction coefficient can be calculated from the absorption coefficient, a , by the following equation: $k = a\lambda/4\pi$, where λ is the wavelength of the incident photons. The spectra of n show an increasing trend with increasing energy of the incident photons and varied in the range of 1.5–2.2 in the near UV–Vis region, as seen in Fig. 10b. The fundamental electron excitation is given by a complex dielectric constant. It has two components, the real and imaginary, which are connected with n and k values. Therefore, the complex dielectric function (ϵ_1) is related to the complex refractive index by the following equations:

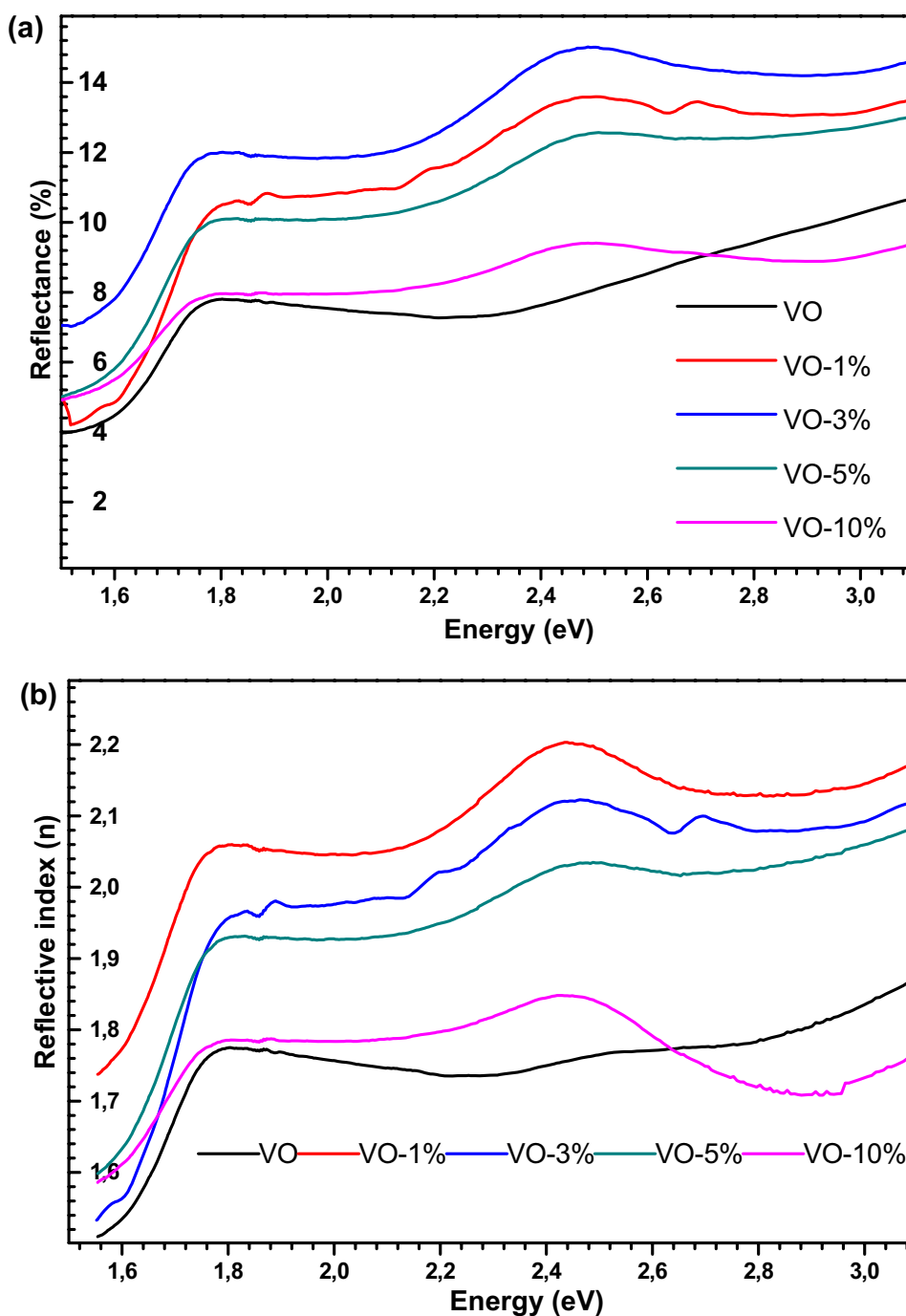
$$\epsilon_1 = (n^2 + k^2) \quad (9)$$

and

$$\epsilon_2 = 2nk, \quad (10)$$

where $n(\omega)$ and $k(\omega)$ are frequency-dependent refractive index (n) and extinction coefficient (k), respectively. The variations of the real and imaginary parts of dielectric constant dependent on the energy of incident photons are indicated in Fig. 11. As seen in Fig. 11a, while the spectral behavior of the refractive index is dominant on the variation of the real dielectric constant, the imaginary dielectric constant has a spectral behavior as a variation of extinction coefficient which is given in inset of Fig. 11b. The minimum and maximum values of ϵ_1 varies between 2.2 and 4.9, respectively. The value of ϵ_2 has limits of 0.1–0.9 in the visible region.

Fig. 10 The reflectance spectra (a) and refractive index (b) of the V₂O₅ thin films as a function of photon energy ($h\nu$)

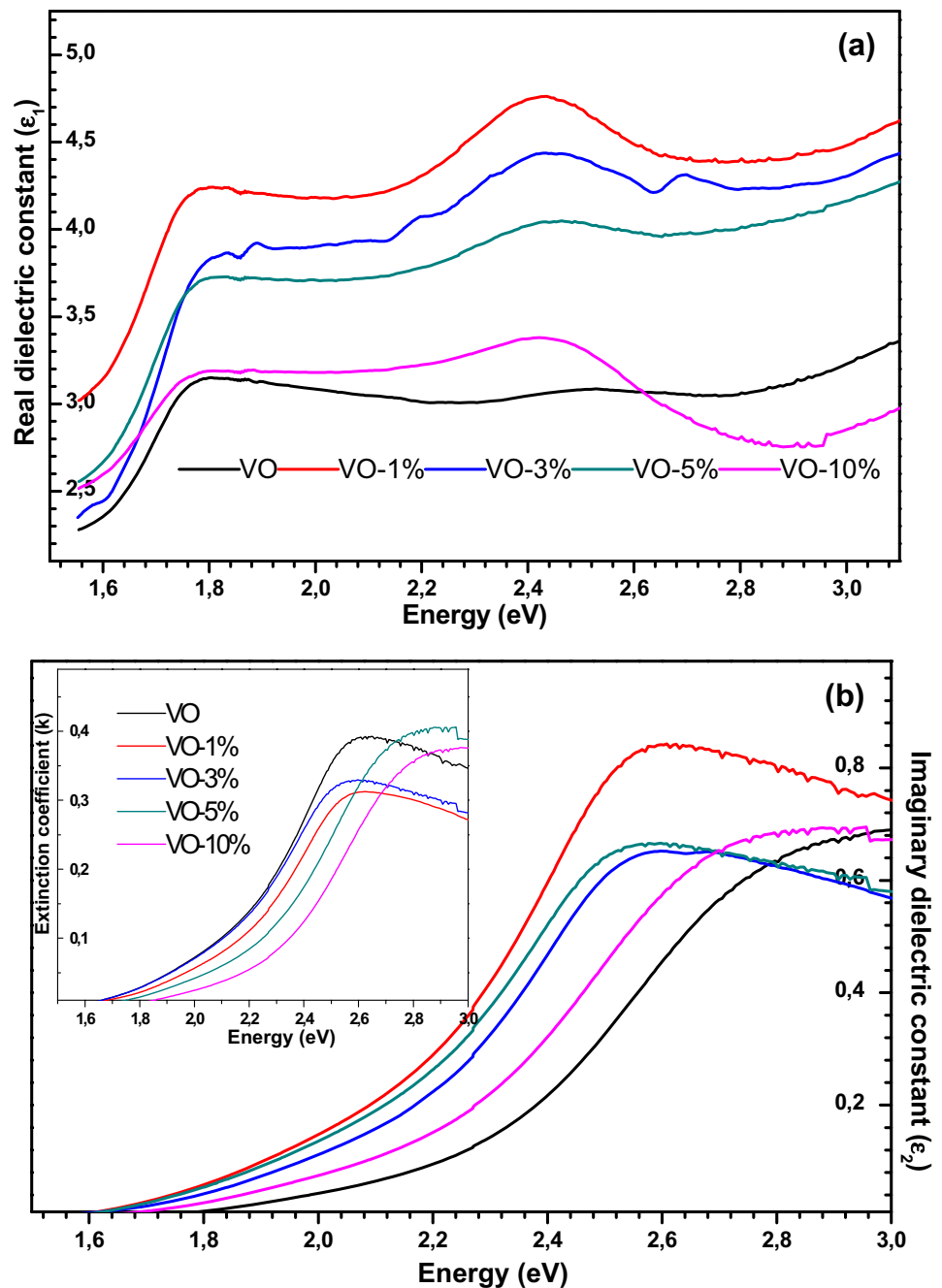


4 Conclusion

In conclusion, the nanostructured films of W-doped V₂O₅ were successfully deposited by the spray pyrolysis technique. Besides, formation, morphological variation, structural and optical properties of nanostructured V₂O₅ films were explained in detail. The XRD patterns demonstrated mainly three different crystal structures of monoclinic VO₂, orthorhombic V₂O₅ and tetragonal V₂O₅. The W dopant caused change of the phase with reducing

monoclinic VO₂ with increasing dopant ratio and mixture phase of α - and β -V₂O₅ phase is obtained at 10 wt% W. The SEM and the AFM images show that the undoped film prepared using basic precursor solution at 400 °C annealing temperature formed with small-sized nanostructural morphology, while enhancing nanostructural morphology has been clearly seen in the films obtained with the different ratios of the W dopant at the same experimental condition. In addition to the SEM and the AFM measurements, the Raman spectra suggested that the surface

Fig. 11 The real (a) and imaginary (b) parts of the dielectric constant of the V_2O_5 thin films as a function of photon energy ($h\nu$). Inset shows a plot of extinction coefficient versus photon energy



diffusion phenomenon which plays an important role in the growth process of nanorods due to high dependence on the oxygen absorption is enhanced with the W dopant. The PL spectra show PL quenching in the W-doped V_2O_5 nanorods, indicating surface states with increasing length of the nanorods may act as traps and thereby may decrease excitonic emission. Furthermore, the optical absorbance, transmittance and reflectance spectra with the related graphs demonstrated the changed electronic behaviors such as band gap, reflective index and dielectric constants.

References

1. N. Singh, A. Umar, N. Singh, H. Fouad, O.Y. Alotman, F.Z. Haque, Highly sensitive optical ammonia gas sensor based on Sn doped V_2O_5 nanoparticles. *Mater. Res. Bull.* **108**, 266–274 (2018)
2. H. Liu, Y. Gao, J. Zhou, X. Liu, Z. Chen, C. Cao, H. Luo, M. Kanehira, Growth of oriented vanadium pentaoxide nanostructures on transparent conducting substrates and their applications in photocatalysis. *J. Solid State Chem.* **214**, 79–85 (2014)

3. M. Liu, B. Su, Y. Tang, X. Jiang, A. Yu, Recent advances in nanostructured vanadium oxides and composites for energy conversion. *Adv. Energy Mater.* **7**, 1700885 (2017)
4. D. Wang, D.K. Elumalai, M.A. Mahmud, M. Wright, M.B. Upama, K.H. Chan, C. Xu, F. Haque, G. Conibeer, A. Uddin, V₂O₅-PEDOT: PSS bilayer as hole transport layer for highly efficient and stable perovskite solar cells. *Org. Electron.* **53**, 66–73 (2018)
5. M.Y. Ameen, P. Shamjid, T. Abhijith, V.S. Reddy, Solution processed transition metal oxide anode buffer layers for efficiency and stability enhancement of polymer solar cells. *Opt. Mater.* **75**, 491–500 (2018)
6. S. Vadnala, N. Paul, A. Agrawal, S.G. Singh, Enhanced infrared sensing properties of vanadium pentoxide nanofibers for bolometer application. *Mater. Sci. Semicond. Process.* **81**, 82–88 (2018)
7. D.X. Long, Y. Xu, S.J. Kang, W.T. Park, E.Y. Choi, Y.C. Nah, C. Liu, Y.Y. Noh, Solution processed vanadium pentoxide as charge injection layer in polymer field-effect transistor with Mo electrodes. *Org. Electron.* **17**, 66–76 (2015)
8. Y. Qin, L. Zhao, M. Cui, “Ultrathin vanadium pentoxide nanobelt for ethanol-sensing applications: experimental and ab initio study. *J. Alloys Compd.* **735**, 1480–1487 (2018)
9. E. Eren, C. Alver, G.Y. Karaca, E. Uygun, L. Oksuz, A.U. Oksuz, High-performance flexible complementary electrochromic device based on plasma modified WO₃ nano hybrids and V₂O₅ nanofilm with low operation voltages. *Electroanalysis* **30**, 1–12 (2018)
10. Z. Liu, H. Zhang, Q. Yang, Y. Chen, Graphene/V₂O₅ hybrid electrode for an asymmetric supercapacitor with high energy density in an organic electrolyte. *Electrochim. Acta* **287**, 149–157 (2018)
11. K.Y. Pan, D.H. Wei, Enhanced electronic and electrochemical properties of core-shelled V₂O₅-Pt nanowires. *Appl. Surf. Sci.* **427**, 1064–1070 (2018)
12. S. Iwanaga, M. Marciniak, R.B. Darling, F.S. Ohuchi, Thermopower and electrical conductivity of sodium-doped V₂O₅ thin films. *J. Appl. Phys.* **101**, 123709 (2007)
13. K. McColl, I. Johnson, F. Cora, Thermodynamics and defect chemistry of substitutional and interstitial cation doping in layered a-V₂O₅. *Phys. Chem. Chem. Phys.* **20**, 15002 (2018)
14. B. Etemadi, J. Mazloom, F.E. Ghodsi, Phase transition and surface morphology effects on optical, electrical and lithiation/delithiation behavior of nanostructured Ce-doped V₂O₅ thin films. *Mater. Sci. Semicond. Process.* **61**, 99–106 (2017)
15. A. Gies, B. Pecquenard, A. Benayad, H. Martinez, D. Gonbeau et al., Effect of silver co-sputtering on V₂O₅ thin films for lithium micro batteries. *Thin Solid Films* **516**, 7271–7281 (2008)
16. M.S. Renard, N. Emery, R. Baddour-Hadjean, J.P. Pereira-Ramos, γ'-V₂O₅: a new high voltage cathode material for sodium-ion battery. *Electrochim. Acta* **252**, 4–11 (2017)
17. R. Irani, M.S. Rozati, S. Beke, Structural and optical properties of nanostructural V₂O₅ thin films deposited by spray pyrolysis technique: effect of the substrate temperature. *Mater. Chem. Phys.* **139**, 489–493 (2013)
18. N.M. Abd-Alghafour, N.M. Ahmed, Z. Hassan, M. Bououdina, High-performance p–n heterojunction photodetectors based on V₂O₅ nanorods by spray pyrolysis. *Appl. Phys. A* **122**, 817 (2016)
19. M. Mousavi, M. Kompany, N. Shahtahmasebi, M.M. Bagheri-Mohagheghi, Study of structural, electrical and optical properties of vanadium oxide condensed films deposited by spray pyrolysis technique. *Adv. Manuf.* **1**, 320–328 (2013)
20. M. Przesniak-Welenc, M. Lapinski, T. Lewandowski, B. Koscieliska, L. Wicikowski, W. Sadowski, The influence of thermal conditions on V₂O₅ nanostructures prepared by sol–gel method. *J. Nanomater.* **2015**, 1–8 (2015)
21. Y. Wang, Z. Li, X. Sheng, Z. Zhang, Synthesis and optical properties of V₂O₅ nanorods. *J. Chem. Phys.* **126**, 164701 (2007)
22. G. Pan, J. Yin, K. Ji, X. Li, X. Cheng, H. Jin, J. Liu, Synthesis and thermochromic property studies on W doped VO₂ films fabricated by sol–gel method. *Sci. Rep.* **7**, 6132 (2017)
23. S. Lu, Z. Xue, Y. Chen, F. Wan, Q. Zhu, G.S. Zakharova, Researches on the structure and electrochemical properties of Mo_xV_{2–x}O_{5+y} nanosheets. *Ionics* **23**, 2855 (2017)
24. T.M. Westphal, C.M. Cholang, C.F. Azevedo, E.A. Moura, D.L. da Silva et al., Influence of the Nb₂O₅ doping on the electrochemical properties of V₂O₅ thin films. *J. Electroanal. Chem.* **790**, 50–56 (2017)
25. M. Mousavi, GhH Khorrami, A. Kompany, ShT Yazdi, Structural, optical and electrochemical properties of F-doped vanadium oxide transparent semiconducting thin films. *Appl. Phys. A* **123**, 755 (2017)
26. S. Kredentser, L. Bugaeva, A. Derzhypolski, D. Cherepanov et al., Stability criteria for aqueous colloidal vanadium pentoxide suspensions doped with magnetite nanoparticles. *Colloids Surf. A Physicochem. Eng. Asp.* **506**, 774–781 (2016)
27. S.Y. Zhan, C.Z. Wang, K. Nikolowski, H. Ehrenberg, G. Chen, Y.J. Wei, Electrochemical properties of Cr doped V₂O₅ between 3.8 V and 2.0 V. *Solid State Ion.* **180**, 1198–1203 (2009)
28. J. Zheng, Y. Zhang, X. Jing, Q. Wang, T. Hu, N. Xing, C. Meng, Improvement of the specific capacitance of V₂O₅ nanobelts as supercapacitor electrode by tungsten doping. *Mater. Chem. Phys.* **186**, 5–10 (2017)
29. Y. Chen, W.D. Liang, H. Xu, Effect of Mo on phase transition temperature of VO₂ nanopowders. *Mater. Res. Innov.* **14**(2), 173–176 (2010)
30. Z. Wan, H. Mohammad, Y. Zhao, R.B. Darling, M.P. Anantram, Bipolar resistive switching characteristics of thermally evaporated V₂O₅ thin films. *IEEE Electron Device Lett.* **39**, 9 (2018)
31. C.V. Ramana, R.J. Smith, O.M. Hussain, C.M. Julien, On the growth mechanism of pulsed-laser deposited vanadium oxide thin films. *Mater. Sci. Eng. B* **111**, 218–225 (2004)
32. M. Panagopoulou, D. Vernardou, E. Koudoumas, D. Tsoukalas, Y.S. Raptis, Oxygen and temperature effects on the electrochemical and electrochromic properties of rf-sputtered V₂O₅ thin films. *Electrochim. Acta* **232**, 54–63 (2017)
33. S.V. Grayli, G.W. Leach, B. Bahreyni, Sol–gel deposition and characterization of vanadium pentoxide thinfilms with high TCR. *Sens. Actuators A* **279**, 630–637 (2018)
34. C. Drosos, C. Jia, S. Mathew, R.G. Palgrave, B. Moss, A. Kafizas, D. Vernardou, Aerosol-assisted chemical vapor deposition of V₂O₅ cathodes with high rate capabilities for magnesium-ion batteries. *J. Power Sources* **384**, 355–359 (2018)
35. S. Thiagarajan, M. Thaiyan, R. Ganesan, Physical properties exploration of highly oriented V₂O₅ thin films prepared by electron beam evaporation. *New J. Chem.* **39**, 9471–9479 (2015)
36. R. Irani, S.M. Rozati, S. Beke, Effects of the precursor concentration and different annealing ambients on the structural, optical, and electrical properties of nanostructured V₂O₅ thin films deposited by spray pyrolysis technique. *Appl. Phys. A* **124**, 321 (2018)
37. N. Abd-Alghafour, N.M. Ahmed, Z. Hassan, S.M. Mohammad, M. Bououdina, M. Ali, Characterization of V₂O₅ nanorods grown by spray pyrolysis technique. *J. Mater. Sci. Mater. Electron.* **27**, 4613–4621 (2016)
38. C. Batista, R.M. Ribeiro, V. Teixeira, Synthesis and characterization of VO₂-based thermochromic thin films for energy-efficient windows. *Nanoscale Res. Lett.* **6**, 301 (2011)
39. I. Pradeep, E.R. Kumar, N. Suriyanaranan, Ch. Srinivas, N.V. Rao, Structural, optical and electrical properties of pure and Fe doped V₂O₅ nanoparticles for junction diode fabrications. *J. Mater. Sci. Mater. Electron.* **29**, 9840–9853 (2018). <https://doi.org/10.1007/s10854-018-9024-1>

40. W. Xue-Jin, L. Yu-Ying, L. De-Hua, F. Bao-Hua, H. Zhi-Wei, Q. Zheng, Structural and optical properties of tungsten-doped vanadium dioxide films. *Chin. Phys. B* **22**(6), 066803 (2013)
41. N.J. Ridha, F.K.M. Alosfur, M.H.H. Jumali, S. Radiman, Dimensional effect of ZnO nanorods on gas-sensing performance. *J. Phys. D Appl. Phys.* **51**, 43 (2018)
42. B. Balamuralitharan, I.H. Cho, J.S. Baka, H.J. Kim, V_2O_5 nanorod electrode material for enhanced electrochemical properties by a facile hydrothermal method for supercapacitor applications. *New J. Chem.* **42**, 11862–11868 (2018)
43. J. Lee, Y. Wu, Z. Peng, Hetero-nanostructured materials for high-power lithium ion batteries. *J. Colloid Interface Sci.* **529**, 505–519 (2018)
44. D. Mukherjee, D. Das, A. Dey, A.K. Mallik, J. Ghosh, A.K. Sharma, A.K. Mukhopadhyay, Evaluation of temperature-dependent microstructural and nanomechanical properties of phase pure V_2O_5 . *J. Sol-Gel Sci. Technol.* **87**, 347–361 (2018). <https://doi.org/10.1007/s10971-018-4745-4>
45. M. Ugurlu, B. Alim, I. Han, L. Demir, Delocalization and charge transfer studies of PERMENDUR49, KOVAR and Ti50Co50 alloys from relative K X-ray intensity ratios. *J. Alloys Compd.* **695**, 2619–2627 (2017)
46. A.A. Mane, M.P. Suryawanshi, J.H. Kim, A.V. Moholkar, Superior selectivity and enhanced response characteristics of palladium sensitized vanadium pentoxide nanorods for detection of nitrogen dioxide gas. *J. Colloid Interface Sci.* **495**, 53–60 (2017)
47. W.J. Yan, M. Hu, J.R. Liang, D.F. Wang, Y.L. Wei, Y.X. Qin, Preparation and room temperature NO_2 -sensing performances of porous silicon/ V_2O_5 nanorods. *Chin. Phys. B* **25**(4), 040702 (2016)
48. C. Marini, E. Arcangeletti, D. Di Castro, L. Baldassare, A. Perucchi, S. Lupi, S. Malavasi, L. Boeri, E. Pomjakushina, K. Conder, P. Postorino, Optical properties of $V_{1-x}Cr_xO_2$ compounds under high pressure. *Phys. Rev. B* **77**, 235111 (2008)
49. N.M. Abd-Alghafour, N.M. Ahmed, Z. Hassan, M.A. Almessiere, M. Bououdina, N.H. Al-Hardan, High sensitivity extended gate effect transistor based on V_2O_5 nanorods. *J. Mater. Sci. Mater. Electron.* **28**, 1364–1369 (2017)
50. W.-J. Yan, M. Hu, J.-R. Liang, D.-F. Wang, Y.-L. Wei, Y.-X. Qin, Preparation and room temperature NO_2 -sensing performances of porous silicon/ V_2O_5 nanorods. *Chin. Phys. B* **25**, 040702 (2016)
51. S. Rajeshwari, J.S. Kumar, R.T. Rajendrakumar, N. Ponpandian, P. Thangadurai, Influence of Sn ion doping on the photocatalytic performance of V_2O_5 nanorods prepared by hydrothermal method. *Mater. Res. Express* **5**, 025507 (2018)
52. K. Sieradzka, D. Wojcieszak, D. Kaczmarek, J. Domaradzki, G. Kiriakidis, E. Aperathitis, V. Kambalafka, F. Placido, S. Song, Structural and optical properties of vanadium oxides prepared by microwave-assisted reactive magnetron sputtering. *Opt. Appl.* **41**, 1–7 (2011)
53. R.K. Sharma, P. Kumar, G.B. Reddy, Synthesis of vanadium pentoxide (V_2O_5) nanobelts with high coverage using plasma assisted PVD approach. *J. Alloys Compd.* **638**, 289–297 (2015)
54. N.M. Abd-Alghafour, N.M. Ahmed, Z. Hassan, Fabrication and characterization of V_2O_5 nanorods based metal–semiconductor–metal photodetector. *Sens. Actuators A* **250**, 250–257 (2016)
55. K.Y. Pan, D.H. Wei, Optoelectronic and electrochemical properties of vanadium pentoxide nanowires synthesized by vapor-solid process. *Nanomaterials* **6**, 140 (2016)
56. A. Dey, M. Kumar Nayak, A.C. Mary Esther et al., Nanocolumnar crystalline vanadium oxide-molybdenum oxide antireflective smart thin films with superior nanomechanical properties. *Sci. Rep.* **6**, 36811 (2016)
57. A.S. Hassanien, A.A. Akl, Effect of Se addition on optical and electrical properties of chalcogenide CdSSe thin films. *Superlattices Microstruct.* **89**, 153–169 (2016)
58. D. Vick, L.J. Friedrich, S.K. Dew, M.J. Brett, K. Robbie, M. Seto, T. Smy, Self-shadowing and surface diffusion effects in obliquely deposited thin films. *Thin Solid Films* **339**, 88–94 (1999)

Publisher's Note Springer Nature remains neutral with regard to jurisdictional claims in published maps and institutional affiliations.